

Exploring the Photorefractive Effect in Polymer-Dispersed Liquid Crystals Using Near-Field Scanning Optical Microscopy

Jeffrey E. Hall and Daniel A. Higgins*

Department of Chemistry, Kansas State University, Manhattan, Kansas 66506

Received: August 19, 2003; In Final Form: October 18, 2003

Static and dynamic near-field scanning optical microscopy (NSOM) methods are used to study physical phenomena associated with photorefractivity in dye-doped polymer dispersed liquid crystals (PDLCs). Micrometer-sized liquid crystal droplets doped with perylene and *N,N'*-dioctyl-1,4,5,8-naphthalene diimide (NDI) dyes, which serve as the photoexcitable electron donor and acceptor, respectively, are studied. The droplets are encapsulated within a thin poly(vinyl alcohol) film. Simultaneously recorded topographic, fluorescence, and birefringence NSOM images show the films to be morphologically complex, containing ellipsoidal and collapsed ellipsoidal droplets. The presence of the collapsed droplets suggests the dissolved dyes may be surface active. Nevertheless, the NSOM images prove the vast majority of dye is contained within the well-defined liquid crystal droplets. Data on the local ion migration and liquid crystal reorientation dynamics is obtained by dynamic NSOM imaging methods. A sinusoidally modulated electric field is applied across the sample, between the aluminized NSOM probe and the electrically conductive film substrate. Lock-in detection of the modulated optical signal resulting from field-induced liquid crystal reorientation is used to obtain amplitude and phase images of the sample. Comparison of the images recorded before, during, and after photogeneration of ions shows spatial variations in the relative importance of ion generation and migration on the liquid crystal orientation state. Computer simulations of the field-dependent ion migration dynamics and the liquid crystal response are used to better understand the data obtained.

Introduction

Photorefractive materials are being explored for possible use in a number of emerging technologies, including optical data storage¹ and processing,² security verification methods,³ and various medical imaging systems.⁴ Over the years, a number of different photorefractive materials have been developed. Inorganic photorefractives, based on noncentrosymmetric crystalline systems such as LiNbO₃, were the first to be investigated.⁵ Soon afterward, it was realized that these materials are difficult to process and exhibit relatively weak photorefractivity.^{4,6} As a result, a number of research groups began developing organic-polymer- and small-molecule-based solid-state organic photorefractives.^{7–9} These organic systems are designed to incorporate photoexcitable electron donors and acceptors and charge transporting media (i.e., conjugated polymers) to allow for efficient charge generation and separation. Importantly, they also include strong nonlinear optical chromophores, which yield enhanced photorefractivity.

The solid-state materials described above often rely on electronic polarization (via the Pockel effect) of the photorefractive gain medium to achieve a modulated refractive index. Therefore, the magnitude of the photorefractive response is somewhat limited and usually requires the application of large DC electric fields.^{4,10} A number of methods for achieving enhanced photorefractivity are currently being explored. These include incorporation of plasticizers and highly polarizable chromophores into the photorefractive medium.^{4,6} In a particularly promising alternative approach, several research groups have recently undertaken the development of liquid-crystal-based

photorefractives.^{11–15} These materials take advantage of the fact that many liquid crystals are strongly birefringent and, as liquids, are readily reoriented (usually via the Kerr effect) by relatively small electric fields. Consequently, much greater refractive index modulation and stronger photorefractivity can usually be achieved.^{11,16}

Liquid-crystal-based photorefractives can be prepared by sandwiching common nematic liquid crystals (doped with suitable electron donor and acceptor dyes) between optically transparent electrodes.^{11,17} Such systems have exhibited some of the largest photorefractive gains to date.⁴ One disadvantage of these materials, however, arises from the limited resolution that can be achieved in the refractive index profile. The resolution limit arises from the increase in elastic energy that accompanies distortion of the liquid crystal alignment over short distances.^{4,18} Polymer-supported liquid crystals (PSLCs)¹⁵ and polymer-dispersed liquid crystals (PDLCs)^{18,19} have been suggested as materials that can overcome this resolution limit by “dividing” the liquid crystalline phase into a number of independent regions. Importantly, the liquid crystal in PSLCs and PDLCs is still readily reoriented by relatively small electric fields, and such materials still yield large photorefractive responses. Unfortunately, because PDLC films are typically comprised of micrometer-sized liquid crystal droplets dispersed in an optically transparent polymer, they exhibit complicated spatial variations in the dynamical phenomena associated with photorefractivity.²⁰ To fully understand the photorefractive process in PDLCs (and PSLCs), detailed knowledge of the local charge generation and migration dynamics, and the local mechanism by which liquid crystal orientational relaxation occurs is required.

* Corresponding author. E-mail: higgins@ksu.edu.

Near-field scanning optical microscopy (NSOM) methods^{21–26} provide a valuable set of tools that can be used to better understand the photorefractive effect in dye-doped PDLCs. NSOM allows for the simultaneous recording of high-resolution topographic images and sub-diffraction-limited optical images of such materials.²⁷ While spatial resolution in optically thick samples is often limited by far-field contrast,²⁷ the simultaneous acquisition of optical and topographic information provides a means by which sample morphology can be directly related to other film properties deduced from the optical images, including those associated with photorefractivity. Numerous optical contrast mechanisms can be used to simultaneously record a number of different optical images,^{21–26} greatly enhancing the wealth of chemical and physical information available.

We have previously employed static and dynamic NSOM imaging methods in studies of both undoped and dye-doped PDLC materials.^{27–30} A detailed understanding of local PDLC film properties is now emerging from these studies and from previous bulk^{31–37} and microscopic³⁸ investigations of similar materials. It is now clear that electric field-induced liquid crystal reorientation dynamics in PDLC films are highly complex, varying spatially within and between individual droplets.³⁹ Our NSOM and far-field optical studies have shown that liquid crystal reorientation is more difficult to induce in outer equatorial droplet regions.^{28,38} Liquid crystal relaxation upon removal of an applied field is also fastest in these same regions.³⁸ These results point to a greater elastic restoring force near the droplet surface, where there is increased nematic phase distortion.^{35,36} Effective orientational anchoring of the interfacial liquid crystal may also play a role.^{35,40} Liquid crystal reorientation dynamics have also been observed to vary across central droplet regions.^{28,38}

While knowledge gained in these previous studies has been used to better understand the dynamics in undoped PDLC systems, the data is also relevant to the mechanisms by which dye-doped PDLCs exhibit photorefractivity.²⁰ These previous results suggest the photorefractive response in dye-doped PDLCs is both spatially and temporally complex. Such complexity arises from both spatial variations in the liquid crystal response to an applied electric field and variability in the relevant ion generation and migration dynamics.

In the present publication, previously developed static and dynamic NSOM imaging methods^{27,29,41,42} are used for the first time to better understand the photorefractive effect in dye-doped PDLCs. The materials selected for study have been previously shown to exhibit some of the largest photorefractive gains observed to date.^{11,15} A complete understanding of photorefractivity in these materials requires elucidation of the physical film morphology, local film optical properties, and the local rates of ion migration and liquid crystal reorientation, both of which are reflected in the dynamic optical response of the PDLC droplets to applied fields. Simultaneous topographic, birefringence, and fluorescence imaging of photorefractive PDLC films is used to better understand droplet shape, liquid crystal organization, the location of the dye dopants within the film, and the influence of these dopants on the droplet structure. In dynamic NSOM studies, simultaneously recorded amplitude and phase images of the modulated optical birefringence signal resulting from AC field-dependent reorientation of the liquid crystal are used to characterize the local dynamics associated with photorefractivity. Finally, computer simulations are used to help derive conclusions from the NSOM data. These simulations are performed for a simplified one-dimensional model of the probe–sample–substrate system. Finite difference

time domain (FDTD) methods are used to solve the necessary differential equations describing field-dependent ion migration and liquid crystal reorientation. Simulated optical signals derived from this model closely mimic the experimentally obtained NSOM data.

Experimental Section

Materials. Photorefractive PDLC thin films were prepared from dye-doped liquid crystal and an aqueous solution of poly-(vinyl alcohol) (PVA). The liquid crystal employed (E7) was purchased from Merck and used as received. E7 is an eutectic mixture of cyanobiphenyls and terphenyls. PVA (9000 M_w , 80% hydrolyzed) was purchased from Aldrich and purified by dialysis against several portions of ultrapure water (18 $M\Omega$ cm). Perylene dye was obtained from Aldrich and used as received. *N,N'*-Dioctyl-1,4,5,8-naphthalene diimide (NDI) was synthesized as described previously.⁴³ The two dyes were incorporated into the liquid crystal by first dissolving them in a small amount of chloroform and then adding the chloroform solution to the liquid crystal. The chloroform was allowed to evaporate by letting the solution stand overnight. The final dye concentrations in the liquid crystal were 2.3 mM for perylene and 7.0 mM for NDI. The dye-doped liquid crystal was then emulsified in a 3% (by weight) aqueous PVA solution, yielding a 3% (by weight) liquid crystal suspension. A few drops of this emulsion were then spin cast onto a clean ITO-coated (20 Ω/cm^2) glass microscope slide and the solvent was allowed to evaporate. The films were dried overnight prior to use. Electrical connection was made to the ITO slide using silver paint and fine transformer wire.

Methods. Static near-field optical birefringence, fluorescence, and topographic images were all recorded using a modified TM-Microscopes Aurora NSOM. This instrument has been described previously.⁴⁴ NSOM fiber probes were produced in house.⁴⁴ The probes were mounted to quartz-crystal tuning forks (32 kHz). Tip–sample separation was maintained at approximately 5 nm by tuning-fork-detected shear-force feedback.⁴⁵

For simultaneous birefringence and fluorescence imaging, 514 nm light from an argon ion laser and the doubled output (at 435 nm) of a Coherent Mira 900-F Ti:sapphire laser were simultaneously coupled into the NSOM probe fiber. Halfwave and quarterwave plates were used to set the polarization state of the 514 nm light at the probe tip. Linearly polarized light was obtained from the tip with polarization purity of greater than 90%. The 435 nm light was elliptically polarized. As the sample was raster scanned beneath the probe, both the 514 nm light transmitted through the sample and perylene fluorescence excited in the sample were collected using a microscope objective (Nikon, 0.8 numerical aperture). The 514 nm light collected was reflected from a dichroic short pass filter, passed through a Glan-laser polarization analyzer, and imaged onto a photomultiplier tube (PMT). The analyzer was set to pass light polarized perpendicularly to that exiting the probe aperture in the absence of sample birefringence. The perylene fluorescence passed through the dichroic short-pass filter and was imaged onto a single photon counting avalanche photodiode (APD). Residual 435 nm light was blocked using a 475 nm long-pass filter, while residual 514 nm light was blocked using a holographic notch filter. After conversion of the photon counts from the APD to a voltage, both the PMT and APD signals were fed into the analogue inputs of the microscope control electronics.

Electric-field-induced liquid crystal reorientation dynamics and ion migration dynamics were studied using this same microscope. Figure 1 shows a simplified schematic of the

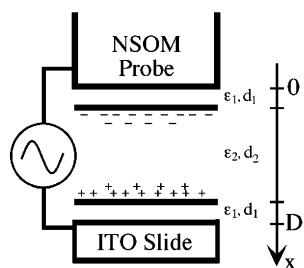


Figure 1. Simplified schematic of the probe-sample-substrate geometry. One-dimensional computer simulations of the experimental data (see text) are based on this model. The NSOM probe is assumed to be in contact with the polymer film (dielectric constant $\epsilon_1 = 11$, thickness $d_1 = 20$ nm) covering a liquid crystal droplet ($\epsilon_2 = 19$, $d_2 = 1$ μm).

experimental geometry. In these experiments, a modulated electric field was applied between the aluminum-coated probe and the ITO-coated substrate using a standard digital waveform generator. Electrical connection was made to the end of the aluminum-coated probe using silver paint and fine transformer wire. Care was taken to ensure the aluminum-coated probe was electrically insulated from the tuning fork. The 633 nm light from a He-Ne laser was coupled into the probe fiber (in place of 514 nm light) as a means to monitor the liquid crystal orientation state. Electron transfer between the perylene and NDI dopants was initiated by coupling 488 nm light from an argon ion laser into the NSOM probe fiber (in place of 435 nm light). Typically, ≈ 150 μW of 633 nm light and ≈ 200 μW of 488 nm light were coupled into the fiber simultaneously. Under these conditions, the power at 488 nm from the NSOM probe was ≈ 50 – 100 pW. The 633 nm light was linearly polarized at the probe tip (polarization purity greater than 90%), while the 488 nm light was elliptically polarized. The transmitted 633 nm light was reflected from a dichroic short-pass, through the polarization analyzer and onto the PMT. Residual 488 nm light was blocked using a holographic notch filter. The modulated PMT signal resulting from field-induced liquid crystal reorientation was fed into a lockin amplifier (EG&G). The amplitude and phase signals from the lockin, detected at the second harmonic of the modulated field, were fed into the microscope control electronics and used directly in the recording of dynamic images. A sinusoidally modulated (50–400 Hz) waveform was employed to induce ion and liquid crystal dynamics in all imaging experiments.

Results and Discussion

Static NSOM Imaging. Figure 2 shows simultaneously recorded topographic, birefringence, and fluorescence images of a perylene and NDI-doped PDLC film. Asymmetric two-beam coupling experiments have previously been used to demonstrate efficient photorefractivity in these materials.^{11,46} As depicted by the topographic image (Figure 2A), these thin films are morphologically complex, containing ellipsoidal and collapsed ellipsoidal droplets. The birefringence image (Figure 2B) indicates the liquid crystal is predominantly entrapped within these droplets. Importantly, the strong birefringence patterns observed for the droplets indicate the dissolved dyes have not substantially disrupted the liquid crystalline order. Such images are also routinely used to deduce the liquid crystal organization within the individual droplets.⁴⁷ In these materials, the liquid crystal in ellipsoidal droplets assumes the well-known “bipolar” configuration.⁴⁰ In the collapsed ellipsoids, a range of different configurations are observed.⁴⁸ The fluorescence image (Figure 2C) proves that the perylene (and also NDI)

remains dissolved primarily in the liquid crystal droplets. That is, the dyes have not been substantially dispersed in the polymer by the action of polymer micelles present in the aqueous PDLC emulsion used in film preparation. The fluorescence is very weak in this image because of the strong electron-transfer quenching of perylene fluorescence by NDI.^{11,46}

The formation of the collapsed ellipsoidal droplets occurs spontaneously (i.e., it is not tip induced)⁴⁹ and is reminiscent of the “pseudo-toroidal” PDLC droplets created by addition of surfactant to aqueous PVA/liquid-crystal emulsions prior to film casting.⁴⁸ The presence of the collapsed droplets in the current studies is, therefore, consistent with possible (weak) surfactant-like behavior of the dye dopants (especially NDI). Dye molecules adsorbed at the polymer/liquid-crystal interface may weaken the polymer shell covering the droplet, causing it to collapse under certain circumstances. The importance of such droplet shape variations has been demonstrated previously.^{31,35,36,38} Highly shaped droplets exhibit markedly different reorientation dynamics than do spheroidal ones. Specifically, liquid crystal relaxation between the field-aligned and zero-field states is significantly faster in collapsed droplets.^{31,35,36,38} Hence, the observed droplet shape variations lead to spatial heterogeneity in the reorientation dynamics and the photorefractive response of the sample.

Dynamic NSOM Imaging. The dynamics of field-induced liquid crystal and dye-dopant reorientation have been explored previously in our labs, using dynamic NSOM and far-field optical methods,^{27,29,38,41,42} and by other groups using different spectroscopic techniques.^{31–37} The purpose of the present work is to better understand dynamical processes of direct relevance to photorefractivity in dye-doped PDLC films. In particular, new information on the buildup of the local space-charge field within individual liquid crystal droplets is sought, along with information on the dynamics of liquid crystal reorientation under the influence of this local field.

Dynamic NSOM imaging experiments were conducted by applying a sinusoidally modulated electric field between the NSOM probe and the conductive substrate upon which the sample was supported. In undoped PDLC samples, this modulated field produces a time-dependent modulation of the liquid crystal orientation state. In dye-doped samples it also induces reorientation of the dyes (i.e., via host-guest interactions and/or direct molecule-field interactions).²⁸ When dissolved ions are present (whether permanent or photogenerated transient ions), the applied electric field also causes these ions to migrate to/from the polymer/liquid-crystal interface. The buildup and decay of charged interfacial double layers modifies the local field within the droplet in time, causing a change in the orientation state of the liquid crystal.

The ion migration dynamics and the liquid crystal reorientation dynamics are detected optically in these experiments by monitoring the field-modulated birefringent state of the liquid crystal. The optical signal is obtained by simply detecting the light transmitted through the sample under crossed polarization conditions. Application of the modulated electric field then results in a modulated optical signal for which the amplitude and phase characteristics are strongly dependent on the local concentration of ions and the viscoelastic properties of the particular droplet being interrogated (i.e., as in eq 5). Importantly, because the modulated electric field is applied with the sharp, metalized NSOM probe, the dynamics induced in the droplet often occur in confined volumes, near the NSOM probe. Hence, high-resolution contrast (i.e., from the near-field) has

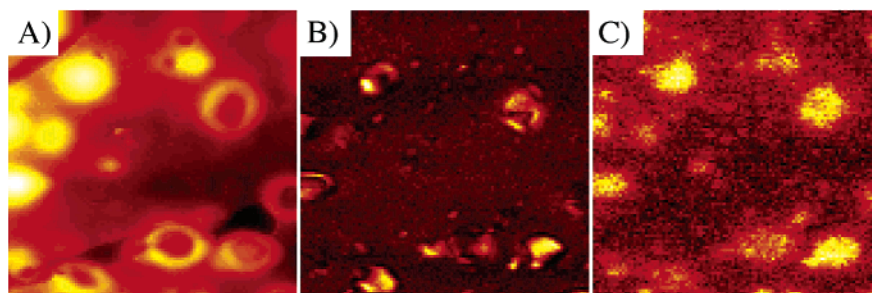


Figure 2. (A) Topographic, (B) birefringence, and (C) fluorescence images of a perylene- and NDI-doped photorefractive PDLC thin film ($20 \times 20 \mu\text{m}$ area).

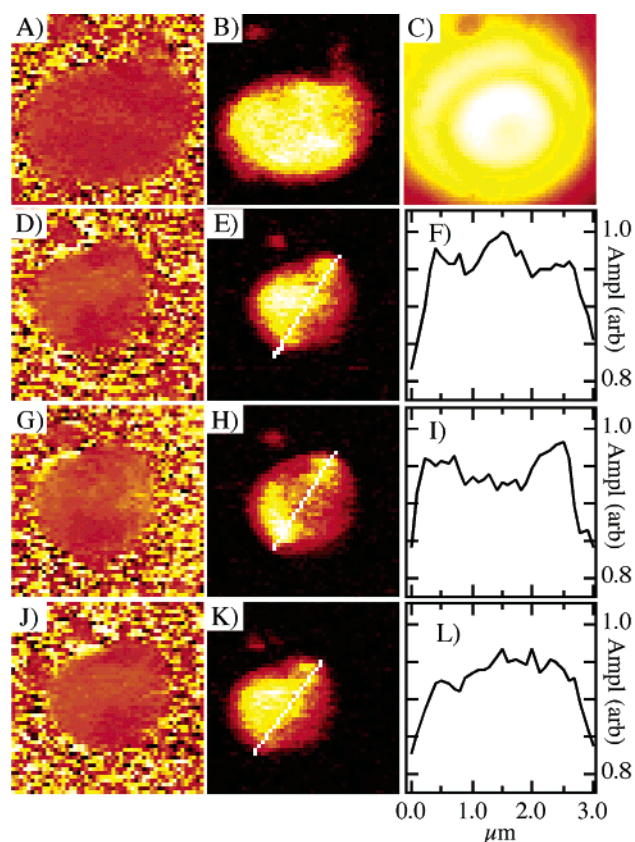


Figure 3. (A) Phase, (B) amplitude, and (C) topographic images of an $\approx 4.5 \mu\text{m}$ diameter undoped liquid crystal droplet. (D) Phase and (E) amplitude images of an $\approx 3 \mu\text{m}$ diameter dye-doped droplet imaged using 633 nm light. (F) Line scan from the amplitude image in (E). (G) Phase and (H) amplitude images of the same droplet shown in (D) and (E) but imaged using 633 nm light, while exciting the perylene dissolved in the droplet by simultaneous illumination through the probe at 488 nm. (I) Line scan from the amplitude image in (H). (J) Phase and (K) amplitude images recorded using 633 nm light only. (L) Line scan from the amplitude image in (K). Images (J) and (K) were recorded after exposure to 488 nm light during collection of images (G) and (H).

been observed in previous dynamic NSOM experiments, and might also be expected in the present studies.²⁷

Figure 3 shows the results of dynamic NSOM imaging experiments on both undoped and dye-doped PDLC droplets. The liquid crystal dynamics in all experiments were monitored using 633 nm light, which is not expected to induce electron transfer between perylene and NDI. Images of the samples were recorded before, during, and after photogeneration of ions. Ion generation was accomplished by simultaneous illumination of the sample with 488 nm light coupled through the NSOM probe. Again, 633 nm light was employed to detect the field-modulated liquid crystal dynamics. Attempts to record images by optically

chopping the 488 nm light (i.e., at 20 Hz) failed because of the slow buildup (tens of milliseconds or more) and decay of the photogenerated ions.

Figures 3A–C depict NSOM phase, amplitude, and topographic images of an undoped ellipsoidal PDLC droplet imaged using 633 nm light only. Figures 3D–L show data from a dye-doped ellipsoidal droplet recorded (I) prior to illumination at 488 nm (Figures 3D–F), (II) during 488 nm illumination (Figures 3G–I), and (III) after illumination at 488 nm. Again, optical contrast in all these images was obtained using 633 nm light. The phase and amplitude images provide a direct means for observing spatial variations in the liquid crystal reorientation dynamics in both the presence and absence of ions.^{27,28,30}

The phase images provide the simplest means for observing variations in the dynamics within individual droplets. Contrast in the amplitude images is more complicated and depends strongly on the optical thickness of the local droplet region and the alignment of the local optical axis relative to the incident and detected polarizations. Variations in these parameters primarily lead to a change in the signal-to-noise ratio of the phase images. Phase images of both the undoped and dye-doped droplets show contrast consistent with spatial variations in the dynamics of liquid crystal reorientation.^{27,28,30,38} For example, the phase images of the doped droplet depicted in Figure 3 show a measurable decrease in the phase angle (darkening of the image) near the apparent “poles” (disclination points) of the bipolar liquid crystal configuration. Such contrast is consistent with slower relaxation dynamics near the droplet poles, as observed previously.^{27,38}

Comparison of the phase images for the doped and undoped droplets yields new information on the effect of the dissolved dyes and/or ions on the liquid crystal dynamics. The mean phase angle over the undoped droplet was found to be $168^\circ \pm 1^\circ$. For the doped droplet, prior to 488 illumination, a mean phase angle of $177^\circ \pm 1^\circ$ was measured. Here, (and below), the error bars reported represent 95% confidence intervals. While direct comparison of the phase data between droplets is made difficult by possible differences in the field strength within the different droplets (i.e., due to polymer shell thickness variations, etc.), and due to differences in droplet size and shape, these data depict the general trend observed between doped and undoped droplets. Specifically, the phase angle is larger on average in the droplets of the dye-doped samples. In undoped samples, the relaxation process is governed by the viscoelastic properties of the liquid crystal droplet alone. In the presence of ions, the electric field strength within the droplet varies in time as the ions migrate to form and/or reform charged double layers.⁴¹ As the concentration of ions increases, the relative importance and rate of this second mechanism increase. The phase angle differences between the doped and undoped droplets are consistent with faster relaxation of the liquid crystal due to incorporation of some ions in the doped PDLC droplets prior to initial 488 nm

illumination. Exposure of the sample to light during preparation and/or its mounting in the microscope are likely sources of these ions.

Upon illumination of the doped droplet with 488 nm light, an additional change in the phase angle was observed. Since these images were recorded on the same droplet, conclusions based on these differences are far more reliable than when different droplets are compared. The mean phase angles determined from Figures 3D,G,I are, respectively, $177^\circ \pm 1^\circ$ (488 off), $181^\circ \pm 1^\circ$ (488 on), and Figure 3I $177^\circ \pm 1^\circ$ (488 off again). Statistically significant differences in the phase angle were seldom observed for undoped droplets in otherwise identical experiments. The increase in phase angle observed during photogeneration of ions (488 on) indicates that the liquid crystal reorientation dynamics are faster under such circumstances, as expected. Interestingly, the phase image of the doped droplet also appears to become more uniform during ion generation. Such a result might be expected if the dynamics are controlled to a greater extent by space-charge field formation and decay, at the higher ionic concentrations. It is also likely these local field dynamics have a different (and possibly more uniform) lateral spatial dependence than the elastic relaxation mechanism. Finally, the return of the phase angle to its original value in the final image (Figure 3J) indicates that the majority of ions generated during exposure to 488 nm light are neutralized by back electron transfer or some other process.

The amplitude images for the doped droplet (see Figures 3E,H,K) also show detectable changes upon exposure to 488 nm light, consistent with photogeneration of ions within the droplet. Figures 3F,I,L present line scans taken from these amplitude images. The line scans depict the changes most clearly. Prior to 488 nm illumination, the amplitude signal across the droplet is peaked near the droplet center (see Figure 3F). Then, during 488 nm illumination, the amplitude signal over the center of the droplet decreases relative to that in outer droplet regions (compare Figures 3F and 3I). The observed amplitude decrease is consistent with faster liquid crystal relaxation due to an increased rate of field decay at higher ion concentrations. The spatial dependence of this decrease can be attributed partly to spatial variations in the relative roles played by ion migration and droplet viscoelastic properties in governing the reorientation dynamics. Unfortunately, due to the dependence of the amplitude signal on the local droplet optical properties, it is difficult to draw detailed conclusions on such spatial variations from the amplitude images. However, the change in amplitude over the center of the droplet is consistent with the relatively greater importance of local field dynamics in governing liquid crystal reorientation in central droplet regions. Alternatively, the appearance of the amplitude image under 488 nm illumination might reflect variations in the local rate of ion generation. Clearly, in thicker regions of the droplet, more ions will be generated in time as there is a longer optical path length, and hence, more 488 nm light is absorbed. In reality, these (and other) effects may all contribute simultaneously, yielding a complicated response overall.

As in the series of phase images, after illumination at 488 nm, the amplitude image returns approximately to its original appearance (compare Figures 3F and 3L). The line scans show the center of the droplet again exhibits the largest modulation amplitude. In contrast to the phase data, the amplitude signal appears to decrease from one image to the next (this is commonly observed). This result suggests that permanent (or long-lived) ions are produced. These are subsequently randomly dispersed (laterally) throughout the droplet. Unfortunately, the

amplitude images suffer from longer-term drift in the efficiency at which the laser (633 nm) is coupled into the probe fiber, making the actual origins of this effect somewhat ambiguous. Since the phase images yield a much more reliable measure of the dynamics, it is apparent that the majority of ions recombine on a time scale shorter than is required to record an image (about 20 min). However, it is also clear from numerous experiments performed on other droplets that some photogenerated ions are very long-lived and may in fact be permanent.

As a final caveat, it should be noted that the photogenerated, reduced form of NDI absorbs strongly near 488 nm.⁵⁰ The resulting increase in absorption at this wavelength could possibly reduce the rate of perylene excitation, and hence charge generation. However, the concentrations of reduced NDI generated in these experiments are believed to be at most tens of micromolar (see below). As a result, the increased absorbance due to this species is negligible, and therefore is believed to have an insignificant effect on the signals recorded above.

Simulations

Computer simulations were undertaken to better interpret the results of the NSOM experiments described above. These simulations were used to model the ion dynamics, the orientational response of the liquid crystal to the local electric field, and the resulting optical signal obtained. FDTD methods were employed in solving the necessary differential equations.

Model. A simplified one-dimensional model for the experimental geometry and the dye/ion-doped liquid crystal droplets was employed. This model is similar to one developed previously for modeling double-layer dynamics in electrochemical systems.⁵¹ Figure 1 shows a schematic of the model. The simulations were performed along a line parallel to the NSOM probe axis and perpendicular to the sample plane. The tip and sample were assumed to be in contact, as were the sample and substrate. Thin polymer films separated the liquid crystal droplet from the probe and substrate surfaces. The aluminum-coated probe and ITO-coated substrates were assumed to behave identically as ideal conductors. Simulations were performed for different initial ion concentrations in order to better understand the effects of ion photogeneration on the liquid crystal dynamics. Prior to application of an electric field, the ions were uniformly distributed throughout the droplet.

In this model, the electrical potential, $\phi(x,t)$, (in one dimension) within the sample was determined from the Poisson equation:

$$\frac{\partial^2 \phi(x,t)}{\partial x^2} = -\frac{\rho(x,t)}{\epsilon \epsilon_0} \quad (1)$$

where $\rho(x,t)$ is the charge density (derived from the ion concentration profiles) as a function of position and time, and ϵ is the dielectric constant at each position in the sample. The polymer was taken to be free of ions (i.e., $\rho(x,t) = 0$ in the polymer), while $\rho(x,t)$ was calculated as described below for each position in the doped liquid crystal droplet. The dielectric constant, ϵ_1 , and thickness, d_1 , of the polymer layer were taken to be 11 and 20 nm, respectively. For the purposes of determining the local electric field, the liquid crystal droplet was assumed to behave as an isotropic dielectric, with a dielectric constant, ϵ_2 , of 19 and a diameter, d_2 , of 1000 nm. The usual boundary conditions were employed in solving eq 1. Specifically, $\phi(x = 0, t) = \phi_0(t)/2$ at the tip-sample junction and $\phi(x = D, t) = -\phi_0(t)/2$ at the sample-substrate junction, where $\phi_0(t)$ is the potential waveform applied between the

NSOM probe and substrate, along the x direction, and $D = 2d_1 + d_2$. The requirement that the normal component of the electric displacement be continuous across the polymer/liquid-crystal interface was also employed.

The charge density ($\rho(x,t)$) as a function of time and position within the droplet was determined by implementation of the following equation describing the ion flux within the droplet:^{51,52}

$$J_i(x,t) = -\frac{FE(x,t)}{RT}D_iC_i(x,t)z_i - D_i\frac{\partial C_i(x,t)}{\partial x} \quad (2)$$

where $J_i(x,t)$ is the flux of species i (i.e., anions or cations), $E(x,t)$ the local electric field calculated by taking the gradient of $\phi(x,t)$ (from eq 1), D_i the diffusion coefficient of species i , $C_i(x,t)$ its local concentration, and z_i its charge. F is the Faraday Constant, R is the gas constant, and T is temperature. The diffusion coefficients for the photogenerated, singly charged (i.e., $z_i = \pm 1$) cations and anions were assumed to be identical ($D_i = 3.0 \times 10^{-8} \text{ cm}^2/\text{s}$).¹⁰ The initial ion concentration, $C_i(x,t = 0)$, was varied to simulate the NSOM results described above. The first term on the right in eq 2 describes field-induced ion migration, while the second describes diffusive ion flux. Fick's Second Law was then employed to determine the concentration profile of each ion in the droplet from the ion flux determined above:⁵²

$$\frac{\partial C_i(x,t)}{\partial t} = -\frac{\partial J_i(x,t)}{\partial x} \quad (3)$$

Finally, the concentration profile for each ion was employed to obtain the charge density profile, and hence, the electrical potential profile (via eq 1):

$$\rho(x,t) = F \sum_i z_i C_i(x,t) \quad (4)$$

Once the electric field as a function of time and position within the droplet was obtained (from the gradient of $\phi(x,t)$), further modeling was employed to determine the time-dependent response of the liquid crystal. As described previously,^{35,36} the following differential equation was used to model the local nematic director dynamics as a function of position within the droplet:

$$\gamma \frac{\partial \theta(x,t)}{\partial t} - k \frac{\partial^2 \theta(x,t)}{\partial x^2} + R \sin(2(\theta(x,t) - \theta_0)) = \frac{\Delta \epsilon \epsilon_0}{2} E^2(x,t) \sin(2\theta(x,t)) \quad (5)$$

The three terms included on the left side of this equation describe (I) the viscous torque density that dampens orientational motions, (II) the local elastic restoring torque density that describes collective liquid crystal motions, and (III) a "bulk" restoring torque density used to incorporate droplet shape factors³⁶ into the model. The latter term is required to drive relaxation in nonspheroidal droplet models³⁶ for which interfacial anchoring of the liquid crystal has been ignored, as is the case here. The right side of the equation describes the field-induced torque on the nematic phase.

In eq 5, $\theta(x,t)$ is the angle the local nematic director makes with respect to the sample plane (perpendicular to the applied field) and θ_0 is the corresponding angle prior to application of the electric field. A small initial tilt angle ($\theta_0 \approx 0.04 \text{ rad}$) is assumed at the start of the simulation (i.e., the liquid crystal is

assumed to be initially aligned nearly parallel to the sample plane). The parameter γ is the rotational viscosity of the liquid crystal ($\gamma = 0.04 \text{ kg m}^{-1} \text{ s}^{-1}$),³⁶ k is the elastic constant for the nematic phase ($k = 1 \times 10^{-11} \text{ N}$),³⁶ R the bulk droplet elastic restoring torque constant ($R = 125$),^{27,36} and $\Delta \epsilon$ the dielectric anisotropy of the liquid crystal ($\Delta \epsilon = 14$). In general, γ may vary near the droplet surface. For the purposes of the present simulation, however, it was taken to be constant.

The simulations were started at zero field and were run through the appropriate number of field modulation cycles required to achieve equilibrium behavior (i.e., until the liquid crystal reorientation dynamics yielded the same results from cycle to cycle). Typically this involved simulating greater than 10 field cycles. Data from earlier cycles were discarded.

Simulation Results. Figure 4 presents representative results from these simulations. The initial ion concentrations are defined in the discussion of the individual results, as is the peak potential applied between the probe and substrate (ϕ_0) in each simulation. These parameters were selected to yield data that best reproduced the trends observed in the NSOM data. For sinusoidal electric field simulations, a frequency of 400 Hz was employed.

Figures 4A and 4B show the anion and cation concentration profiles, respectively, as a function of time and position within the droplet. The profiles during one complete field cycle are shown for half the droplet (due to the symmetry of this simplified model). The initial ion concentration was $30 \mu\text{M}$, and the peak applied potential (ϕ_0) $\pm 2 \text{ V}$. These results show in detail the field-induced migration of the cations and anions as the applied field is cycled. When the NSOM probe is charged positive, a large excess of anions exists in the first few tens of nanometers from the polymer/liquid-crystal interface nearest the probe. At the same time, there is a substantial deficit of cations in a somewhat larger region. When the NSOM probe is charged negative, cations are in excess near the interface and the anion concentration is depleted. Under most circumstances, the concentrations of the cations and anions in the center of the droplet remain relatively uniform and equal to their initial concentrations. As it takes time for migration of these ions to occur during field cycling, the ion profiles lag the applied field to some extent, depending on their initial concentration, the field strength, and their mobility.

The concentration profiles for the cations and anions determine the local electric field experienced by the liquid crystal at any instant in time, via eq 1. As defined in eq 5, liquid crystal reorientation actually depends on the square of the electric field. Therefore, it is the squared field strength that is plotted in Figure 4C as a function of time and position within the droplet (now for half a field cycle). As is readily apparent from these plots, the squared field strength varies spatially within the droplet in time. Specifically, the field maximum in the center of the droplet occurs earlier in the applied field cycle than it does near the interface. In addition, the field maximum is larger near the droplet surface than in central regions. Such variations in the local field lead to complicated spatial and temporal variations in the liquid crystal reorientation dynamics, as observed in the NSOM experiments.

The orientation state of the liquid crystal is plotted as a function of time and position within the droplet in Figure 4D (for half a field cycle). Peak liquid crystal reorientation clearly occurs earlier in the center of the droplet and later near the interface as a result of the ion migration dynamics. In addition, as expected from the field distribution, reorientation occurs to a greater extent nearest the droplet surface (ignoring interfacial anchoring).^{35,40} However, the decay in the field-aligned orienta-

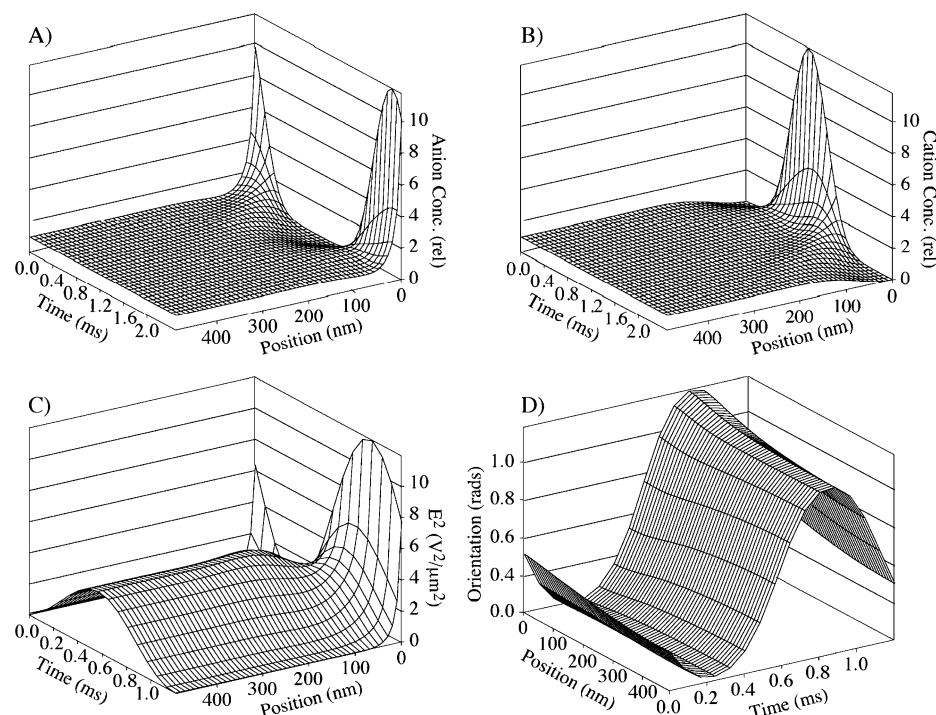


Figure 4. Simulations of the ion, electric field, and liquid crystal reorientation dynamics in a doped PDLC droplet. (A), (B) Local concentrations of anions and cations, respectively, in the droplet as a function of time and position. The concentration profiles are normalized to the original ion concentration. Zero time represents the start of a single cycle of a 400 Hz sinewave (several cycles into the simulation). The data are plotted as a function of distance from the polymer/liquid-crystal interface (at 0 nm). (C), (D) Squared electric field and liquid crystal orientation as a function of time (one-half a field cycle) and position within the droplet. The liquid crystal orientation angle is reported relative to the film plane ($\theta = 0^\circ$).

tion state as a function of distance from the interface is not as significant as might naively be expected. This effect arises from the elastic interactions between the strongly reoriented liquid crystal near the interface and that in the droplet center. Nevertheless, these results indicate that the changes observed in the dynamic NSOM images during photogeneration of ions arise primarily from central droplet regions, and to a lesser extent from the outer circumferential regions. Hence, it may also be concluded that the photorefractive response observed in bulk studies of dye-doped PDLCs is also dominated by field-induced relaxation of the liquid crystal in central droplet regions. As has been shown previously, the dynamics of liquid crystal reorientation are relatively more uniform in central, bulklike droplet regions.^{27,38} Photorefractivity in PDLC-based materials is also expected to be less sensitive to interfacial and near-interfacial effects. Such a conclusion is consistent with the decrease in spatial contrast observed in phase images recorded during photogeneration of ions (see Figure 3G).

The lack of high-resolution (i.e., sub-diffraction-limited) features in the present dynamic NSOM images is likely a direct result of the above phenomenon. Specifically, since the dominant field/ion-dependent differences in the liquid crystal orientation state occur in central droplet regions, much of the optical contrast actually arises from far-field effects. This result contrasts with those of our previous studies of undoped PDLCs in which the dynamics detected occurred primarily in the near-field regime, and hence, high-resolution features were observed.²⁷

Figure 5 shows calculated optical signals derived from three simulations at three different initial ion concentrations: 1 nM, 10 μ M, and 30 μ M. In each case, a peak applied potential of ± 2 V was employed. Again, a 400 Hz sinewave was used. The optical signals were calculated as described previously.²⁸ These simulated optical signals closely resemble those observed on an oscilloscope in actual NSOM experiments.³⁰ As shown in

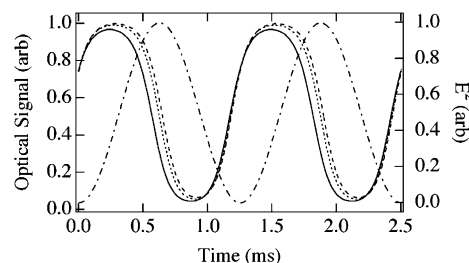


Figure 5. Simulations of the optical signal as a function of time within an ion-doped liquid crystal droplet. Shown are data for ion concentrations of 30 μ M (—), 10 μ M (···), and 1 nM (---), along with the applied, squared electric field (— · — ·).

the data, a phase shift of approximately $+4^\circ$ is observed between the 1 nM and 10 μ M simulations. Likewise, a phase shift of $+12^\circ$ is observed between the 1 nM and 30 μ M simulations. For the data given in Figure 3 (typical of several repeat measurements on different droplets), the experimentally determined phase change between images recorded before and during ion generation was $\approx +4^\circ$. It is therefore concluded that the number of ions generated experimentally is close to that used in these simulations (i.e., $\approx 10 \mu$ M in the droplet center).

Conclusions

Static and dynamic NSOM imaging methods and computer simulations have been used to better understand the dynamical phenomena associated with photorefractivity in dye-doped PDLC thin films. The NSOM data show films of these materials to be morphologically complex. Simultaneously recorded NSOM birefringence and fluorescence images indicate that the dyes and liquid crystal are confined primarily within ellipsoidal and collapsed ellipsoidal droplets. Dynamic NSOM imaging methods show that ion migration and liquid crystal reorientation dynamics can be monitored on submicrometer length scales, and that the

observed dynamics vary spatially within individual droplets. Such effects were attributed to spatial differences in the relative importance of elastic and ion-induced liquid crystal reorientation dynamics. Computer simulations were employed to model the ion dynamics, liquid crystal reorientation, and the optical signals observed in the NSOM experiments. The simulations show that orientational relaxation of the liquid crystal in the presence of ions occurs primarily in central droplet regions. Hence, the dynamics observed become more uniform and less sensitive to interfacial phenomena than in the absence of ions. Taken together, the results of these experimental studies and simulations provide a better understanding of the mechanism by which the photorefractive effect occurs in spatially complex dye-doped PDLC films.

Acknowledgment. The National Science Foundation (CHE-9709034 and CHE-0092225) is thanked for its support of this work. Dr. Aifang Xie is thanked for her helpful comments during preparation of this manuscript.

References and Notes

- (1) Cipparrone, G.; Mazzulla, A.; Nicoletta, F.; Lucchetti, L.; Simoni, F. *Opt. Commun.* **1998**, 297.
- (2) Ono, H.; Kawatsuki, N. *Proc. SPIE* **1998**, 3475, 122.
- (3) Kippelen, B.; Volodin, B.; Meerholz, K.; Javidi, B.; Peyghambarian, N. *Nature* **1996**, 383, 58.
- (4) Zilker, S. *Chem. Phys. Chem.* **2000**, 1, 72.
- (5) Ashkin, A.; Boyd, G. D.; Dziedzic, J. M.; Smith, R. G.; Ballman, A. A.; Levinstein, J. J.; Nassau, K. *Appl. Phys. Lett.* **1966**, 9, 72.
- (6) Moerner, W. E.; Grunnet-Jepsen, A.; Thompson, C. L.; Twieg, R. J. *Appl. Phys. Lett.* **1997**, 70, 1515.
- (7) Moerner, W. E.; Silence, S. *Chem. Rev.* **1994**, 94, 127.
- (8) Yu, L.; Chan, W. K.; Peng, Z.; Gharavi, A. *Acc. Chem. Res.* **1996**, 29, 13.
- (9) Van Steenwinckel, D.; Hendrickx, E.; Persoons, A. *J. Chem. Phys.* **2001**, 114, 9557.
- (10) Wiederrecht, G. *Mol. Supramol. Photochem.* **2001**, 7, 319.
- (11) Wiederrecht, G.; Yoon, B.; Wasielewski, M. *Science* **1995**, 270, 1794.
- (12) Khoo, I. C.; Li, H.; Liang, Y. *Opt. Lett.* **1994**, 19, 1723.
- (13) Ono, H.; Kawatsuki, N. *Recent Res. Dev. Appl. Phys.* **1998**, 47.
- (14) Cipparrone, G.; Mazzulla, A.; Simoni, F. *Mol. Cryst. Liq. Cryst.* **1997**, 299, 329.
- (15) Wiederrecht, G.; Wasielewski, M. *J. Nonlinear Opt. Phys. Mater.* **1999**, 8, 107.
- (16) Khoo, I. C.; Guenther, B. D.; Wood, M. V.; Chen, P.; Shih, M.-Y. *Opt. Lett.* **1997**, 22, 1229.
- (17) Khoo, I. C.; Guenther, B. D.; Slussarenko, S. *Mol. Cryst. Liq. Cryst.* **1998**, 321, 419.
- (18) Golemme, A.; Kippelen, B.; Peyghambarian, N. *Appl. Phys. Lett.* **1998**, 73, 2408.
- (19) Golemme, A.; Kippelen, B.; Maldonado, J.; Peyghambarian, N. *Proc. SPIE* **1998**, 3297, 28.
- (20) Golemme, A.; Kippelen, B.; Peyghambarian, N. *Chem. Phys. Lett.* **2000**, 319, 655.
- (21) Harootunian, A.; Betzig, E.; Isaacson, M.; Lewis, A. *Appl. Phys. Lett.* **1986**, 49, 674.
- (22) Dürig, U.; Pohl, D. W.; Rohner, F. *J. Appl. Phys.* **1986**, 59, 3318.
- (23) Betzig, E.; Trautman, J. K.; Harris, T. D.; Weiner, J. S.; Kostelak, R. L. *Science* **1991**, 251, 1468.
- (24) Vanden Bout, D. A.; Kerimo, J.; Higgins, D. A.; Barbara, P. F. *Acc. Chem. Res.* **1997**, 30, 204.
- (25) Dunn, R. C. *Chem. Rev.* **1999**, 99, 2891.
- (26) Higgins, D. A.; Mei, E. *Near-Field Scanning Optical Microscopy. In Scanning Probe Microscopy and Spectroscopy. Theory, Techniques, and Applications. 2nd ed.*; Bonnell, D., Ed.; Wiley-VCH: New York, 2001; p 371.
- (27) Mei, E.; Higgins, D. A. *J. Chem. Phys.* **2000**, 112, 7839.
- (28) Higgins, D. A.; Liao, X.; Hall, J. E.; Mei, E. *J. Phys. Chem. B* **2001**, 105, 5874.
- (29) Mei, E.; Higgins, D. A. *Appl. Phys. Lett.* **1998**, 73, 3515.
- (30) Mei, E.; Higgins, D. A. *J. Phys. Chem.* **1998**, 102, 7558.
- (31) Drzaic, P. S. *Liq. Cryst.* **1988**, 3, 1543.
- (32) Jain, S. C.; Rout, D. K. *J. Appl. Phys.* **1991**, 70, 6988.
- (33) Jain, S. C.; Thakur, R. S.; Lakshmikumar, S. T. *J. Appl. Phys.* **1993**, 73, 3744.
- (34) Lin, H.; Ding, H.; Kelly, J. R. *Mol. Cryst. Liq. Cryst.* **1995**, 262, 99.
- (35) Erdmann, J.; Doane, J. W.; Zumer, S.; Chidichimo, G. *Proc. SPIE* **1989**, 1080, 32.
- (36) Wu, B.-G.; Erdmann, J. H.; Doane, J. W. *Liq. Cryst.* **1989**, 5, 1453.
- (37) Amundson, K. *Phys. Rev. E* **1996**, 53, 2412.
- (38) Higgins, D. A.; Luther, B. J. *J. Chem. Phys.* **2003**, 119, 3935.
- (39) Higgins, D. A. *Adv. Mater.* **2000**, 12, 251.
- (40) Zumer, S.; Doane, J. W. *Phys. Rev. A* **1986**, 34, 3373.
- (41) Mei, E.; Higgins, D. A. *Appl. Phys. Lett.* **1999**, 75, 430.
- (42) Higgins, D. A.; Mei, E.; Liao, X. *Proc. SPIE* **1999**, 3607, 26.
- (43) Wiederrecht, G.; Svec, W.; Niemczyk, M.; Wasielewski, M. *J. Phys. Chem.* **1995**, 99, 8918.
- (44) Hall, J. E.; Higgins, D. A. *Polym. Mater. Sci. Eng.* **2003**, 88, 186.
- (45) Karrai, K.; Grober, R. *Appl. Phys. Lett.* **1995**, 66, 1842.
- (46) Hall, J. E.; Higgins, D. A. *Rev. Sci. Instrum.* **2002**, 73, 2103.
- (47) Ondris-Crawford, R.; Boyko, E. P.; Wagner, B. G.; Erdmann, J. H.; Zumer, S.; Doane, J. W. *J. Appl. Phys.* **1991**, 69, 6380.
- (48) Springer, G. H.; Higgins, D. A. *J. Am. Chem. Soc.* **2000**, 122, 6801.
- (49) Mei, E.; Higgins, D. A. *Langmuir* **1998**, 14, 1945.
- (50) Greenfield, S. R.; Svec, W. A.; Gosztola, D.; Wasielewski, M. R. *J. Am. Chem. Soc.* **1996**, 118, 6767.
- (51) Feldberg, S. W. *J. Phys. Chem.* **1970**, 74, 87.
- (52) Bard, A. J.; Faulkner, L. R. *Electrochemical Methods: Fundamentals and Applications*; John Wiley and Sons: New York, 1980.